Nuclear Instruments and Methods in Physics Research A 628 (2011) 133–137

Contents lists available at ScienceDirect

Nuclear Instruments and Methods in Physics Research A

journal homepage: www.elsevier.com/locate/nima

A UV sensitive integrated Micromegas with Timepix readout

Joost Melai [a], Amos Breskin [b], Marco Cortesi [b], Yevgen Bilevych [c], Martin Fransen [c], Harry van der Graaf [c], Jan Visschers [c], Victor Blanco Carballo [c], Cora Salm [a,*], Jurriaan Schmitz [a]

[a] MESA+ Institute for Nanotechnology, University of Twente, Enschede, The Netherlands
[b] Weizmann Institute of Science, Rehovot, Israel
[c] NIKHEF, Amsterdam, The Netherlands

ARTICLE INFO

Available online 4 July 2010

Keywords:
Gaseous radiation detector
Micromegas
UV-photon detection
InGrid
CsI photocathode
CMOS post-processing

ABSTRACT

This article presents a detector system consisting of three components, a CMOS imaging array, a gaseous-detector structure with a Micromegas layout, and a UV-photon sensitive CsI reflective photocathode. All three elements have been monolithically integrated using simple post-processing steps. The Micromegas structure and the CMOS imaging chip are not impacted by the CsI deposition. The detector operated reliably in He/isobutane mixtures and attained charge gains with single photons up to a level of 6×10^4. The Timepix CMOS array permitted high resolution imaging of single UV-photons. The system has an MTF50 of 0.4 lp/pixel which corresponds to approximately 7 lp/mm.

1. Introduction

We present a novel integrated gaseous UV-photon detector that is made by post-processing a charge-sensitive CMOS pixel detector. It is based on the InGrid technology [1] which uses microtechnology techniques to construct a Micromegas detector structure on top of the readout chip. This method allows aligning the different components of the detector with the anode plane. The pillars are placed at the intersections of four adjacent pixels; the circular holes in the grid are centered on the input pad of each pixel. The hole pitch equals that of the readout matrix, here 55 μm. The hole diameter can be varied, typical values are 20−30 μm. This affects the optical transparency of the grid, for the range mentioned it is 10–23%. The photosensitivity is obtained by coating the grid with a reflective CsI photocathode [2]. CsI is a very robust photocathode that has been used in combination with many gaseous photon detectors [3]. In Ref. [4] a Micromegas device with a single anode is coupled to a CsI reflective photocathode. A CMOS imaging chip coupled to a non-integrated gaseous electron multiplier (GEM) with a CsI photocathode is described in Ref. [5]. This work presents the first fully monolithic embodiment of such a UV-photon imaging detector.

2. Experimental

The detectors are composed of three elements: the imaging chip, the integrated Micromegas grid, and a reflective photocathode. Fig. 1 shows the full detector assembly. The Micromegas structure, the photocathode and some of the experimental methods discussed below are similar to our earlier work reported in Ref. [6].

The Timepix chip used here [7] is a variant of the Medipix2 chip [8]. It has been designed for the Medipix2 collaboration by CERN, within the EUDET framework. The Timepix chip contains a matrix of 256×256 square pixels with a size of 55 μm. The total imaging area is $\sim14\times14\,mm^2$. Each of the pixels has a large metal input pad connected to an input capacitor. The collected charge is read out with a charge sensitive pre-amplifier capable of detecting charges of less than $1000e^-$. The charge is compared with a threshold value which can be changed per pixel. There are different readout modes. Just as Medipix2, the chip can be used to count the number of hits above a selected threshold during a defined shutter period. In Timepix-mode the arrival time of the first hit above threshold is recorded per pixel, and in TOT-mode (Time Over Threshold) the 14 bit counter is incremented as long as the signal remains above threshold. Because the discharge current of the input capacitor is kept constant at a known value, the TOT readout can be used to measure the input charge.

2.1. Chip post-processing

The detector is built directly on the surface of the imaging chip as described in detail in Ref. [1]. The present devices have been built on single chips, but the process can also be performed on clusters of several chips (for instance a square of 3 by 3 chips) or on entire wafers.

The first step is to cover the anode surface of the pixel matrix with a highly resistive layer, in our case this is a 7 μm Si-rich Si_xN_y layer deposited by plasma-enhanced CVD. This layer protects the

* Corresponding author. Tel.: +31 53 489 2648.
E-mail address: c.salm@utwente.nl (C. Salm).

0168-9002/$ - see front matter © 2010 Elsevier B.V. All rights reserved.
doi:10.1016/j.nima.2010.06.301

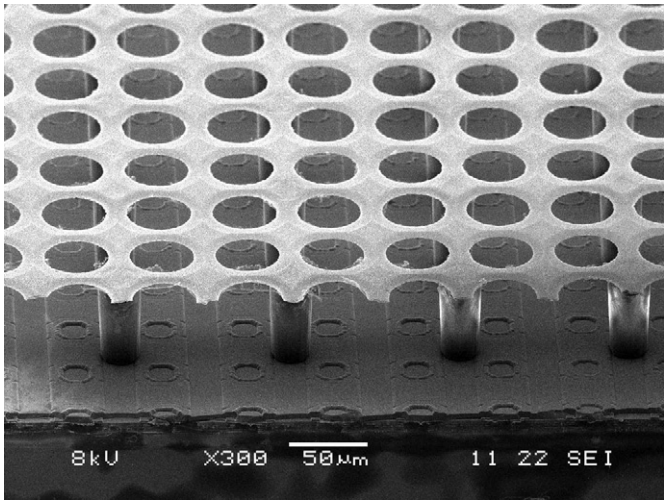

Fig. 1. SEM image of a complete detector with Timepix substrate, highly resistive spark protection layer and InGrid structure with isolating pillars supporting a perforated Al grid.

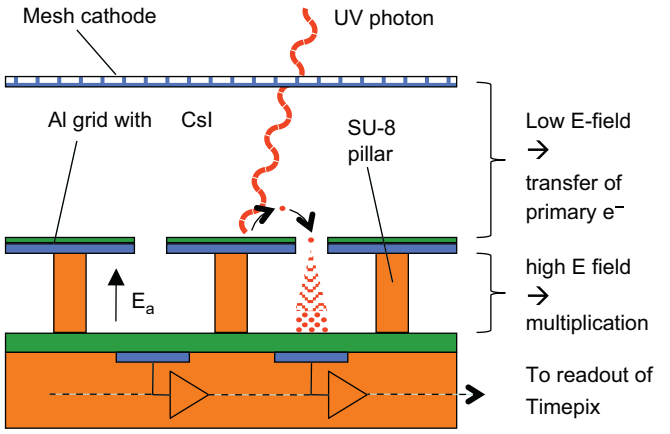

Fig. 2. Illustration of the device and its operation. Light enters through a window from the top; photoelectrons from a CsI photocathode on the grid are focused into the multiplication gap; the resulting avalanche induces charge onto the CMOS pixel array of the Timepix chip, via a discharge-protecting film. Operation was in gas flow mode at 1 atm.

chip by quenching discharges that may occur in the gas during detector operation.

In a next phase the InGrid (Integrated Grid) structure is built. First a photoimagable SU-8 polymer layer is spin cast onto the substrate. This layer is baked to render it solid. A 1 µm thick Al layer is sputtered onto the SU-8. To form the perforated grid the metal is patterned using standard lithography and wet etch techniques. The SU-8 layer, which has already been exposed earlier, is then developed in acetone, removing the unexposed, not crosslinked material from below the grid through the holes in the metal. The structure is rinsed by immersion in iso-propyl alcohol. After drying, the structure appears as shown in Fig. 1. Our present detector has 25 µm diameter holes at a pitch of 55 µm; the multiplication gap (grid-to-anode) is ~80 µm.

The chip is bonded to a readout board. To operate the Timepix chip we further need a small, USB-connected readout module and a PC with dedicated software [9]. The readout board has an integrated gas chamber of approximately $10 \times 10 \times 1.5\,cm^3$. Inside this volume an additional steel cathode mesh is mounted 5–10 mm above the grid. Above this mesh, centered on the location of the chip, is a UV-transparent Suprasil quartz window.

After mounting the chip can be coated with CsI. For this the whole assembly—without the top cover, window and cathode mesh—is placed inside the evaporation chamber. The deposition is done by thermal evaporation in vacuum from a solid CsI source, using resistive heating [2]. In some cases the CsI layer is patterned using a simple Al foil shadow-mask during deposition. The typical CsI thickness is 220 nm.

2.2. Measurement methods

The different elements of the system and the detector operation principle are shown in Fig. 2. Light impinges onto the photocathode layer on the top surface of the grid. The chip surface (anode) is kept at ground potential. The cathode mesh and the grid are typically biased at the same negative potential, to prevent electrons from drifting upwards. The electrons follow the evanescent field of the high field region below the grid. After drifting through the holes the charge is multiplied towards the anode. The charge cloud then falls onto one of the pixels of the matrix.

Charge signals from the detector are recorded from the grid, using a charge preamplifier, a shaping amplifier and a multi-channel analyzer (MCA). The amplifier chain is calibrated by injecting a known charge from a test capacitor. The images are recorded with the Timepix chip, using the readout methods discussed above.

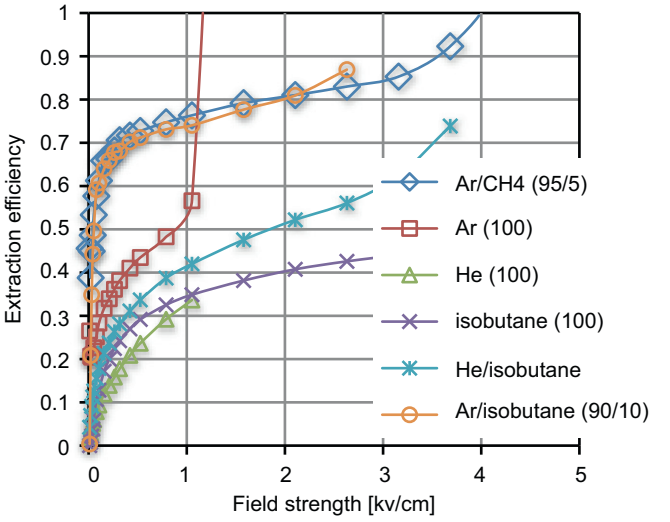

Fig. 3. Extraction efficiency of photoelectrons from a CsI photocathode into various gas mixtures (reference to vacuum). All gases were maintained at 1 atm.

The devices can be operated with different gas mixtures; best results were obtained with a He/isobutane (80/20) mixture. Device operation is very stable in He/isobutane, several detectors have been operated for up to several weeks without any signs of degradation. Lower gains were reached in Ar-based mixtures. There are two drawbacks related to the use of He and isobutane. First, isobutane absorbs UV radiation. For our setup this effect is limited because of the low isobutane concentration and the small thickness of the gas layer (~1 cm). Secondly, in He there is rather high backscattering of photoelectrons on gas molecules compared to other noble gases [10]. This reduces the effective quantum efficiency of the detector, even when mixed with isobutane. Fig. 3 shows the measured extraction efficiency into various gases; this efficiency is the ratio between the extraction levels in gas and in vacuum, at the same bias and irradiation conditions. In He/isobutane (80/20) we reach an extraction level of around 50% for normal operating conditions (~2 kV/cm). For the backscattering in other gas mixtures see Ref. [11].

3. Results and discussion

3.1. Gain as determined from pulse measurements

The gain of the detector was determined by irradiating it with two different sources (UV light and ^{55}Fe). In both cases the grid and the cathode mesh were biased at equal potentials and the anode was grounded; the measurements were done in He/isobutane (80/20) at atmospheric pressure. In one experiment we used an Ar(Hg) lamp with a pinhole aperture placed far from the detector. The light flux was further reduced by means of absorbers. The response of the detector to this irradiation was measured with the pre-amplifier attached to the grid. The exponential pulse-height spectra (typical for single-photon gas avalanche detectors) for a range of bias voltages are shown in Fig. 4a. The distributions are accurately described by Eq. (1), where N is the number of hits, Q is the charge, G is the average gain and C is a constant:

$$N(Q) = C \cdot 1/G \cdot \exp(-Q/G). \quad (1)$$

By making fits to the measured spectra we determined the average gain G for all voltages. We have also determined the gain by measuring the average charge cloud arriving after multiplication of the initial charge from the conversion of ^{55}Fe photons (irradiating through a thin Kapton window) in the gas. The results of both gain measurements are plotted in Fig. 4b. There is good agreement between the two methods; with ^{55}Fe we obtained a slope of 100 V/decade and with UV-photons it is 110 V/decade. The maximum gain that we reached was 6×10^4.

3.2. Spatial resolution using the slanted edge method

To determine the spatial resolution we followed the ISO 12233 procedure [12]. Under UV irradiation images were recorded of the edge of a thin steel sheet placed at a slight angle with respect to the pixel orientation. The response was corrected for fixed patterns, dividing by the data of an open frame (flat-field) measurement taken under the same conditions. The step response was analyzed within a certain Region Of Interest (ROI), as shown

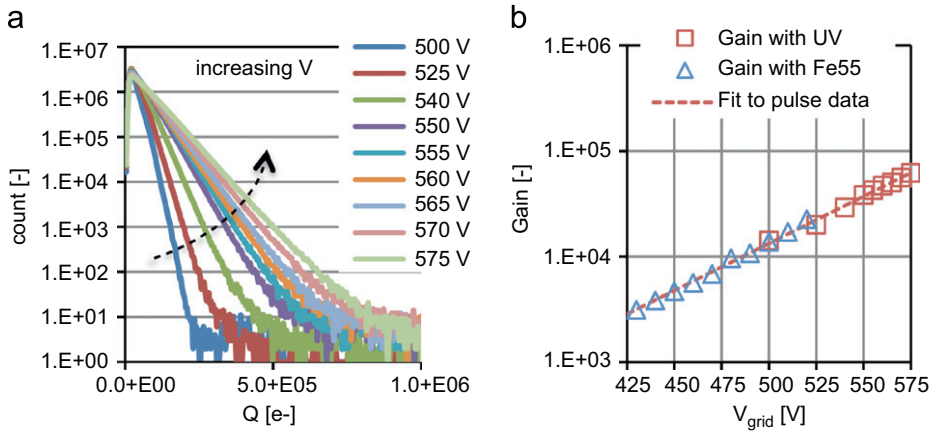

Fig. 4. (a) Pulse-height spectra for a range of bias voltages, recorded on the grid under UV irradiation and (b) Gain vs. bias voltage derived from pulse-height spectra of UV-photons and of ^{55}Fe 5.9 keV X-rays.

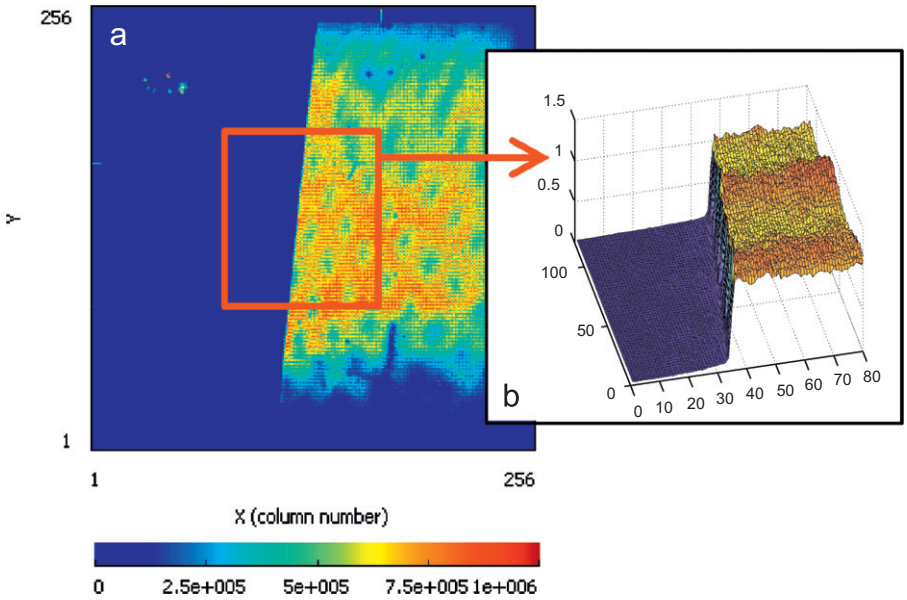

Fig. 5. (a) An image of a slanted metal sheet, the data of a certain ROI are considered, the raw image data are corrected with an open frame measurement taken under the same conditions—providing the step response on the right (b).

in Fig. 5a. For each line of pixels we took the derivative of the pixel counter value and determined the centroid; this defined the edge location within each line of pixels. A linear fit was performed through the centroid locations to derive a description of the edge. The data of all lines were rebinned (in this case with 8 bins per pixel) and simultaneously shifted according to the slant that was determined before. In this way we could combine all data in the ROI in one Edge Step Function (ESF). The derivative of the ESF is the Line Spread Function (LSF). A Gaussian curve was fitted to the LSF; the 1σ spread is 0.48 pixels or 26.4 μm and the FWHM is 1.13 pixels or 62.2 μm. The results are shown in Fig. 6.

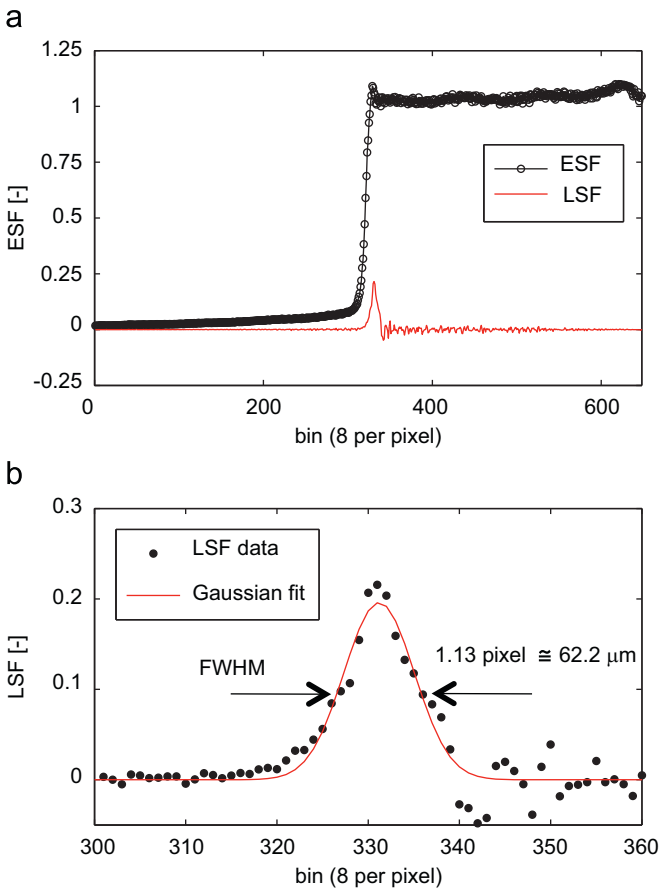

Fig. 6. (a) ESF as derived from the rebinned data within the ROI. (b) LSF data and Gaussian fit.

By performing a Fourier transform of the LSF we obtained the Modulation Transfer Function (MTF) of the entire system. The MTF reaches 50% (MTF50) at 0.4 lp/pixels ($\simeq$ 7 lp/mm). The resolution limit is below the pixel pitch, at the Nyquist frequency MTF = 0.32. The resolution limit is reached at 0.8 lp/pixels ($\simeq$ 14 lp/mm).

3.3. Imaging results

The cathode mesh (see Fig. 2), needed to shape the field above the grid, modulates the light reaching the photocathode. In Fig. 7a we see a Moiré pattern which is the result of using a cathode mesh with a wire pitch of 56 μm and a detector pitch (both grid and readout pads) of 55 μm. Using a coarser mesh, with a pitch of 500 μm, the mesh wires are directly imaged by the detector (Fig. 7b). The high resolution permits observing mesh defects.

The images in Fig. 7 were taken with a partial CsI coating. For experimental reasons not discussed here, the bottom 15% of the matrix were not coated with CsI, which naturally resulted in a lower response in that region.

Fig. 8 shows two images obtained in He/isobutane (80/20) using TOT counting under UV-photon irradiation. Fig. 8(a) is an image recorded with a steel mask of the logo of the University of Twente placed in front of the detector; Fig. 8(b) is an image of a fingerprint intentionally left on the detector window. The latter was obtained by correcting the raw image with the data of an open frame reference image recorded under the same conditions. The fingerprint image was recorded without CsI on the Al grid. This shows that, in spite of the (very) low quantum efficiency, even without CsI the detector performs as a UV imaging device.

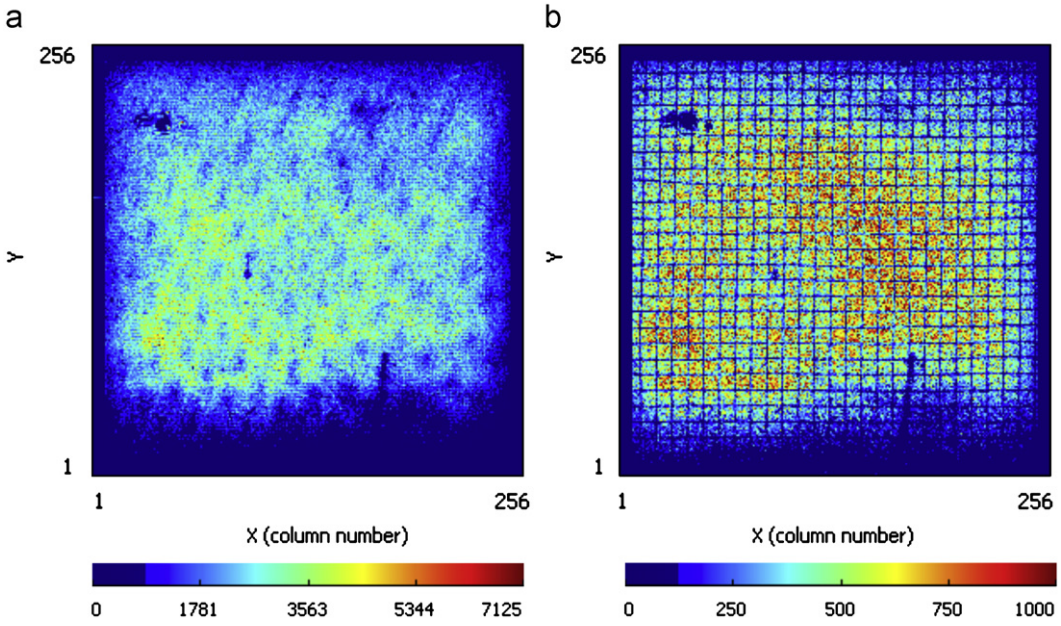

Fig. 7. 2D images of flat-field UV irradiation of the detector shown in Fig. 2 using He/isobutane (80/20) at 1 atm. (a) Moiré pattern resulting from using a 56 μm mesh above the 55 μm pitch detector and (b) direct imaging of the mesh when the mesh pitch is increased to 500 μm.

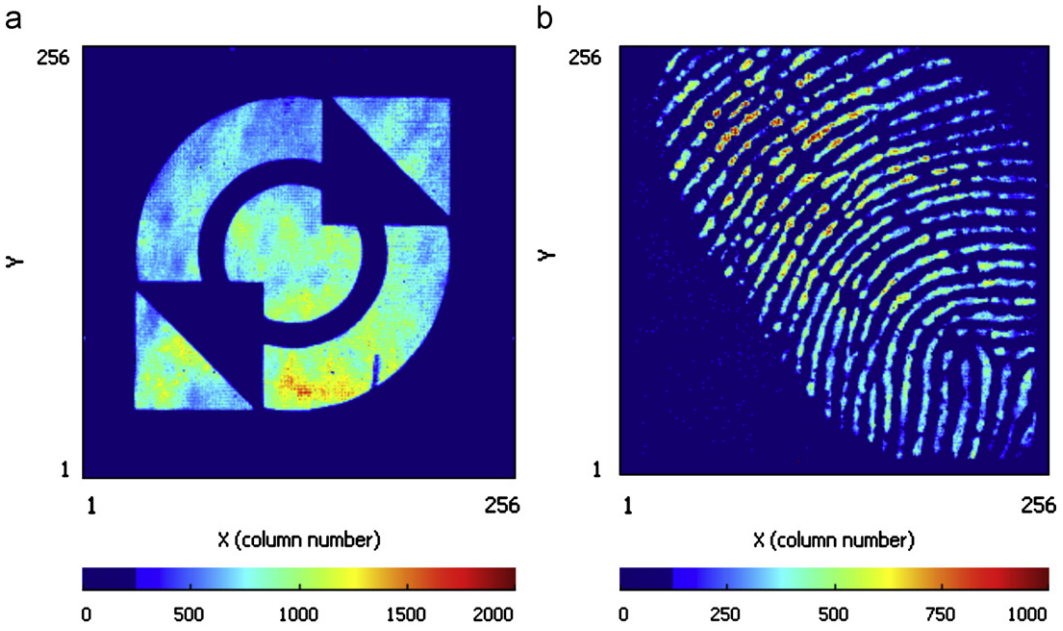

Fig. 8. (a) Image of the logo of the University of Twente and (b) image of a fingerprint left on the detector window.

4. Conclusions

We have presented a monolithic gaseous UV-photon imaging detector with a CsI photocathode. The photocathode deposition and its operation are found to be adequate in combination with both the Micromegas multiplier and with the imaging chip. Most experiments have been performed in He/isobutane (80/20), in which the extraction efficiency is around 50%. The maximum gain that was reached amounts to 6×10^4.

The imaging experiments indicate a good spatial resolution, the LSF has a spread of 26.4 μm, MTF50 is reached at 0.4 lp/pixel ($\simeq 7$ lp/mm). High quality 2D images were recorded.

These encouraging results suggest further investigations directed towards the search for operation conditions and for gas-mixtures assuring better photoelectron collection efficiencies (lower backscattering); investigations of absolute photon detection efficiencies and of ion-blocking (ion-feedback) are foreseen. The new device could find applications in high-resolution imaging of UV-photons. Furthermore, being made of UHV-compatible materials, it could be applicable as a multiplication and readout element also in cascaded visible-light imaging gas photomultipliers [13].

Acknowledgments

The authors acknowledge Sander Smits (of the University of Twente), Max Chefdeville, Fred Hartjes, Joop Rövekamp and Jan Timmermans (all with NIKHEF) and Moshe Klin and Alexey Lyashenko (both from the Weizmann Institute) for their help during the manufacturing of the test devices and the measurements. This research is funded by the Dutch technology foundation STW through project TET-6630. A. Breskin is the W.P. Reuther Professor of Research in The Peaceful Use of Atomic Energy.

References

[1] V.M. Blanco Carballo, et al., IEEE Electron. Dev. Lett. 29 (2008) 585.
[2] A. Breskin, Nucl. Instr. and Meth. A 371 (1996) 116.
[3] R. Chechik, A. Breskin, Nucl. Instr. and Meth. A 595 (2008) 116.
[4] J. Derré, et al., Nucl. Instr. and Meth. A 449 (2000) 314.
[5] R. Bellazzini, et al., Nucl. Instr. and Meth. A 581 (2007) 246.
[6] J. Melai, A. Lyashenko, A. Breskin, H. van der Graaf, J. Timmermans, J. Visschers, C. Salm, J. Schmitz, Nucl. Instr. and Meth. A, in press, doi:10.1016/j.nima.2010.06.165.
[7] X. Llopart, et al., Nucl. Instr. and Meth. A 581 (2007) 485 and its erratum in Nucl. Instr. and Meth. A 585 (2008) 106.
[8] X. Llopart, et al., IEEE Trans. Nucl. Sci. NS-49 (2002) 2279.
[9] T. Holy, et al., Nucl. Instr. and Meth. A 563 (2006) 254.
[10] L.C.C. Coelho, et al., Nucl. Instr. and Meth. A 581 (2007) 190.
[11] J. Escada, et al., J. Instr. 4 (2009) P11025.
[12] P. Burns, D. Williams, in: Proceedings of the PICS 1999, Imaging Science and Technology, 1999, pp. 51–53.
[13] A. Lyashenko, et al., J. Instr. 4 (2009) P07005.